



Cite this: *RSC Adv.*, 2024, 14, 10703

# A new plant-esterase inhibition based electrochemical sensor with signal amplification by MoS<sub>2</sub>@N-CDs for chlorpyrifos detection†

Jiayu Chen,<sup>a</sup> Chun Ji,<sup>b</sup> Xiao Wang,<sup>a</sup> Yunxia Tian<sup>a</sup> and Han Tao  <sup>\*,a</sup>

Chlorpyrifos (CPF) is the most common pesticide entering the food chain and posing a threat to human health. This study presents a new electrochemical biosensor based on molybdenum disulfide nanosheets and nitrogen-doped carbon dot nanocomposite (MoS<sub>2</sub>@N-CDs) and kidney bean esterase (KdBE), and it is shown to achieve accurate detection of CPF. MoS<sub>2</sub>@N-CDs were prepared by a facile solvothermal method and characterized by electron microscopy, X-ray diffraction and X-ray photoelectron spectroscopy. Electrochemical characterization confirmed that MoS<sub>2</sub>@N-CDs facilitated electron transfer and increased the electroactive surface area of the electrode, thereby improved the sensing performance of the electrode. The oxidation peak current of 1-naphthol, which was produced by the hydrolysis of 1-naphthyl acetate catalyzed by KdBE, was adopted as the signal of the sensor. CPF can suppress KdBE activity and consequently cause a decrease in the sensing signal. The experimental results show that the variation of sensing signal is a reliable index to evaluate the CPF level. Under the optimized conditions, the developed enzyme sensor showed superior CPF assay performance with a linear detection range as wide as 0.01–500 µg L<sup>-1</sup> and LOD as low as 3.5 × 10<sup>-3</sup> µg L<sup>-1</sup> (S/N = 3). The inter- and intra-batch RSDs for electrode testing were 4.02% and 2.69%, respectively. Moreover, the developed biosensor also showed good stability and anti-interference. The spiked recoveries of CPF in oilseed rape and cabbage ranged from 98.09% to 106.01% with low relative standard deviation (RSD) (<5.23%), suggesting that the sensor is a promising tool to enable simple, low-cost but highly sensitive large-scale screening of CPF residues in food.

Received 1st January 2024  
Accepted 23rd March 2024

DOI: 10.1039/d4ra00009a

rsc.li/rsc-advances

## 1. Introduction

CPF is an organophosphorus pesticide that has been widely used for pest control in vegetables, fruits, grains and other crops since 1965.<sup>1</sup> CPF is already used in nearly 100 countries, and is likely to be even more widely used in the next 30 years due to food production needs.<sup>2</sup> However, the continued widespread use and abuse of CPF over the years has resulted in it being the most common pesticide entering the food chain and affecting human health.<sup>3</sup> Therefore, there is a huge demand for CPF monitoring, which leads to the urgent need for a simple, low-cost and sensitive CPF detection method.

Currently, multiple quantitative approaches including HPLC,<sup>4</sup> GC-MS/MS,<sup>5</sup> surface-enhanced Raman spectroscopy,<sup>6</sup> fluorescence,<sup>7</sup> magnetic relaxation switching biosensors,<sup>8</sup> enzyme-linked immunosorbent assay<sup>9</sup> and electrochemistry<sup>10</sup>

have been developed for CPF detection. Among them, electrochemical biosensing techniques utilizing the inhibitory effect of CPF on acetylcholinesterase (AChE) activity have emerged as an important tool for trace CPF residual detection.<sup>11,12</sup> Tun *et al.*<sup>13</sup> prepared an AChE-based electrochemical sensor modified with cellulose nanofibers and graphene oxide to implement highly sensitive CPF detection based on the inhibition of CPF on AChE activity. Suwannachat *et al.*<sup>14</sup> constructed an electrochemical biosensor based on AChE and utilized CuNWs and rGO to modify the screen-printed electrode for highly sensitive detection of chlorpyrifos. These methods are undoubtedly simple, fast and highly sensitive. However, AChE is usually acquired from animal blood or tissues with complex extraction and purification steps, which leads to the high cost of AChE, thus greatly limiting its wider application. But, it is gratifying that studies have shown that organophosphorus pesticides can also inhibit the activity of plant esterases.<sup>15,16</sup> More attractively, plant esterases are derived from plants, which are far more accessible, ethical and economical than animals, and the extraction of plant esterases is also easier than that of AChE. Therefore, plant esterases can be utilized as a promising and low-cost alternative enzyme source of AChE for large-scale detection of pesticides detection, but electrochemical studies on plant esterases are currently very scarce.

<sup>a</sup>School of Liquor and Food Engineering, Guizhou Province Key Laboratory of Fermentation Engineering and Biopharmacy, Guizhou University, Huaxi District, Guiyang 550025, China. E-mail: taohanedu@126.com

<sup>b</sup>School of Pharmaceutical Sciences, Guizhou University, Huaxi District, Guiyang 550025, China

† Electronic supplementary information (ESI) available. See DOI: <https://doi.org/10.1039/d4ra00009a>



Moreover, to achieve accurate and reliable assay of trace CPF residues in food, the detection technique needs to be highly sensitive. Employing nanomaterials to enhance the sensitivity of electrochemical sensing platforms is a simple and effective strategy. When nanomaterials are introduced to the electrode surface, their special electronic structure and crystal defects can influence the kinetic process of the electrochemical reaction, resulting in a higher analytical sensitivity. Molybdenum disulfide ( $\text{MoS}_2$ ) nanosheets is another rapidly developing 2D nanomaterial after graphene, which has the advantages of strong adsorption capacity, high reactivity and catalytic performance.<sup>17,18</sup> Moreover, the electron–electron interactions between molybdenum atoms contribute to the enhancement of electron transfer. Hence,  $\text{MoS}_2$  nanosheets are particularly suitable for the development of advanced sensors. Further, compositing  $\text{MoS}_2$  with other functional materials often results in better performance through the advantages of materials complementing each other. Nitrogen-doped carbon dots (N-CDs) is quasi-spherical zero-dimensional carbon nanoparticles with sizes within 10 nm. Studies have demonstrated that N-CDs can improve electrode adsorption capacity, electrocatalytic activity and electrode surface stability.<sup>19</sup> Also, N-CDs is simple to prepare and easy to combine with other materials. As a result, we considered compositing  $\text{MoS}_2$  nanosheets with N-CDs and then using them for functionalized modification of the electrodes, with a view to improving the electrode performance so as to effectively increase pesticide detection sensitivity.

Herein, a new electrochemical sensor was fabricated for the low-cost and high-sensitive detection of CPF. In this sensor, KdBE, which was derived from bean crops widely cultivated worldwide, was used as a susceptible biomolecule for the recognition of CPF. To improve detection sensitivity, as-prepared  $\text{MoS}_2$ @N-CDs nanocomposite was modified on a bare glassy carbon electrode as an electrocatalyst to amplify the electrochemical signals. Subsequently, gold nanoparticles (GNPs) were further decorated on the  $\text{MoS}_2$ @N-CDs-functionalized electrode as a substrate for immobilizing KdBE, and then the outer layer was coated with chitosan, which has good film-forming properties and biocompatibility<sup>20</sup> to prevent enzyme leakage. CPF can hinder the bioactivity of KdBE and decrease the oxidative current signal of 1-naphthol, a product of enzymatic hydrolysis. By monitoring the fluctuation of the electrochemical signal produced by 1-naphthol, simple, low-cost but highly sensitive detection for CPF can be achieved readily. To the best of our knowledge, no study of  $\text{MoS}_2$ @N-CDs in electrochemical sensing has been reported, nor has the detection of CPF with plant esterases been reported.

## 2. Experimental

### 2.1. Materials and reagents

Polyethylene glycol (PEG1000) (AR) was purchased from Shanghai Bioengineering Co., Ltd. Ethylene glycol (99.8%) and thiourea (99%) were purchased from Chongqing Chuandong Chemical Co., Ltd. 1-Naphthyl acetate (1-NA) ( $\geq 99.5\%$ ) and CPF (99%) were obtained from Sigma-Aldrich Co. Ethylenediamine ( $\geq 99.5\%$ ), sodium molybdate ( $\geq 99\%$ ), chlortetracycline ( $\geq 99.9\%$ ), solid blue B (Dye content  $\sim 95\%$ ),  $\text{K}_4[\text{Fe}(\text{CN})_6]$  (99%),

$\text{K}_3[\text{Fe}(\text{CN})_6]$  ( $\geq 99.5\%$ ),  $\text{NaH}_2\text{PO}_4$  (99%), lindane (Analytical Standard) and deltamethrin (Analytical Standard) were purchased from Aladdin Reagents Co., Ltd. Water used throughout all experiments was ultrapure water ( $18.2 \text{ M}\Omega \text{ cm}$ ).

### 2.2. Apparatus

The electrochemical tests were completed by a CHI660E electrochemical analyser (CHI, China), using glassy carbon electrode (GCE) as working electrode,  $\text{Ag}/\text{AgCl}$  electrode as reference electrode and platinum wire as counter electrode. Freeze-drying of KdBE was carried out using a VaCo5 freeze-dryer (Zirbus, Germany). X-ray photoelectron spectroscopy (XPS) was collected on ESCALAB 250Xi (Thermo Fisher Scientific, USA) with an Al  $K\alpha$  radiation source ( $h\nu = 1486.6 \text{ eV}$ ) by pass energy settings of 200 eV (full spectrum) and 50 eV (fine spectrum). X-Ray diffraction (XRD) measurements were performed using an 8 Advance diffractometer (Bruker, Germany) with a voltage of 40 kV, a current of 40 mA, a test range of  $5\text{--}90^\circ$ , and a scanning speed of  $10^\circ \text{ min}^{-1}$ . Scanning electron microscope (SEM) images were acquired using a cold field emission scanning electron microscope SU8010 (Hitachi, Japan) with an accelerating voltage of 10 kV. Transmission electron microscope (TEM) images were obtained from JEM 2100F (JEOL, Japan) with an accelerating voltage of 200 kV. Atomic force microscopy (AFM) was performed by Dimension icon (Bruker, Germany). AFM images of film surface were taken with a scan rate of 1.00 Hz under Tapping mode. The model of probe was Tap300A with  $k = 40 \text{ N m}^{-1}$ .

### 2.3. Preparation of nanomaterials

Preparation of N-CDs: 3.2 mL of ethylenediamine and 2.52 g of citric acid were dissolved in 60 mL of water under magnetic stirring at room temperature. The solution was transferred to a Teflon autoclave and reacted at  $180^\circ \text{C}$  for 5 h. The resulting solution was dialyzed for 24 h and then vacuum dried at  $60^\circ \text{C}$  to obtain N-CDs.

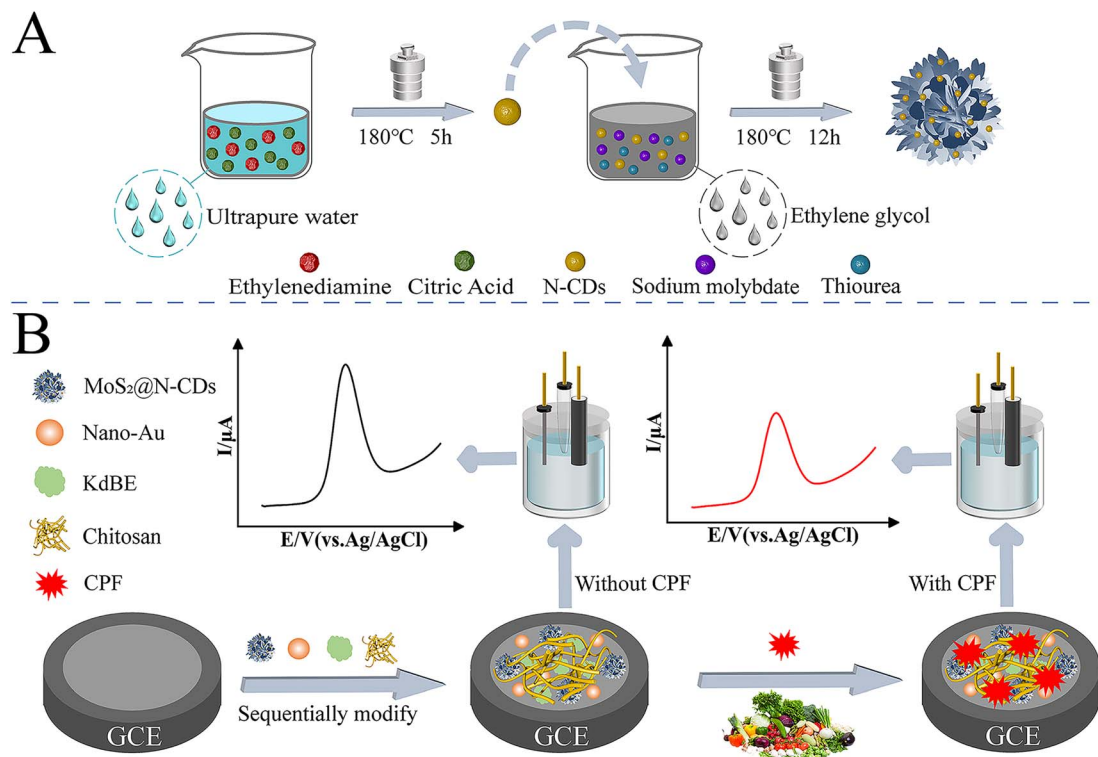
Preparation of  $\text{MoS}_2$ @N-CDs nanocomposite: 0.726 g of sodium molybdate was ultrasonically dispersed in 40 mL of ethylene glycol, then 1.1418 g of thiourea and 0.05 g of N-CDs were added and dispersed uniformly. The resulting solution was transferred to an autoclave and reacted at  $180^\circ \text{C}$  for 12 h. The black product was washed several times with ethanol and water and then dried under vacuum at  $70^\circ \text{C}$  to obtain black  $\text{MoS}_2$ @N-CDs powder.  $\text{MoS}_2$  was prepared with the same method as that of  $\text{MoS}_2$ @N-CDs, except that no N-CDs was added. The preparation process of  $\text{MoS}_2$ @N-CDs is illustrated in Scheme 1A.

Gold colloid were prepared by referring to the method reported previously.<sup>21</sup>

### 2.4. Extraction of KdBE

20 g of kidney bean was ground into powder, then 100 mL of water was poured into and stirred for 30 min. The extract was centrifuged and the supernatant was taken as the crude enzyme solution, which was further purified *via* a two-step bi-aqueous extraction method.<sup>22</sup> Briefly, the first step of extraction is carried out in a two-phase aqueous system consisting of 27% PEG1000 and 13%  $\text{NaH}_2\text{PO}_4$ , and the upper phase was collected after equilibrium of partitioning was reached. Subsequently,





Scheme 1 Schematic diagram of (A) MoS<sub>2</sub>@N-CDs preparation and (B) CPF detection.

(NH<sub>4</sub>)<sub>2</sub>SO<sub>4</sub> (6%) was added to form the second bi-aqueous system, and the lower phase was collected after partitioning. Afterwards, the lower phase was dialyzed in 0.05 mol L<sup>-1</sup> PBS (pH 6.5) for 48 h and then freeze-dried to powder. The image of obtain KdBE is shown in Fig S1.†

### 2.5. Sensor's construction

The surface of GCE was polished with 0.05 μm Al<sub>2</sub>O<sub>3</sub>, followed by ultrasonic cleaning in acetone and water sequentially, and then the cleaned GCE was placed in PBS solution for cyclic voltammetry scanning 10 cycles from 0 V–1 V. After dried in air, 20 μL MoS<sub>2</sub>@N-CDs solution (1.0 mg mL<sup>-1</sup>) was drop-coated on the GCE surface and dried to obtain MoS<sub>2</sub>@N-CDs/GCE. Then, 12 μL gold colloid was further coated on and dried to get Au/MoS<sub>2</sub>@N-CDs/GCE. Subsequently, 10 μL KdBE solution (19.03 U mL<sup>-1</sup>) was dropped onto Au/MoS<sub>2</sub>@N-CDs/GCE surface and dried at 4 °C. Finally, 10 μL 0.25% chitosan solution was covered on the outer layer of the modified electrode to obtain CS/KdBE/Au/MoS<sub>2</sub>@N-CDs/GCE.

### 2.6. Electrochemical measurements

Electrochemical characterization of the electrodes was achieved by cyclic voltammetry (CV) and AC impedance technique in 5.0 mmol L<sup>-1</sup> K<sub>4</sub>[Fe(CN)<sub>6</sub>]/K<sub>3</sub>[Fe(CN)<sub>6</sub>] probe solution. The CV experiments were performed in the potential range of –0.2 ~ 0.7 V with a sweep rate of 0.1 V s<sup>-1</sup>. The frequency range of the AC impedance experiment is 1 Hz–10<sup>5</sup> Hz and the amplitude is 5 mV. To detect CPF, the square wave voltammetry (SWV) technique was used in 0.1 M PBS (pH 7.0) in the range of 0 V–0.8 V. The procedures were as follows: first, the CS/KdBE/Au/MoS<sub>2</sub>@N-CDs/GCE

was placed in 0.1 mol L<sup>-1</sup> PBS containing 0.8 mmol L<sup>-1</sup> 1-NA for SWV testing, corresponding peak current was defined as *I*<sub>0</sub>. After incubation with CPF solutions for 15 minutes, the electrode underwent another SWV test in the same test solution, and the peak current was recorded as *I*<sub>1</sub>. The inhibition rate of peak current was calculated by eqn (1). The schematic diagram of pesticide detection is depicted in Scheme 1B.

$$\Delta I(\%) = (I_0 - I_1)/I_0 \times 100\% \quad (1)$$

## 3. Results and discussion

### 3.1. Characterization of nanomaterials

The morphologies of the prepared nanomaterials were characterized by SEM and TEM. As seen in Fig. 1A, MoS<sub>2</sub> is assembled by many nano-layers, and the layers are stacked with each other to form a flower-like structure, which can increase the specific surface area and facilitate the loading of other materials. Fig. 1B displays the TEM image of N-CDs, revealing spherical particles with an average size of 3.11 nm that are evenly dispersed. Fig. 1C demonstrates that GNPs in gold colloid are also spherical particles with an average size of 9 nm. The inset of Fig. 1C is the absorption spectrum of GNPs, which shows that the absorbance value at 450 nm was 1.06. According to the method reported by Haiss *et al.*<sup>23</sup> the concentration of GNPs can be estimated to be 23.92 nM. Fig. 1D is the SEM image of MoS<sub>2</sub>@N-CDs nanocomposite. It is apparent that the morphology of MoS<sub>2</sub> remained unchanged almost despite complexation with N-CDs. The inset of Fig. 1E shows the selected area electron diffraction





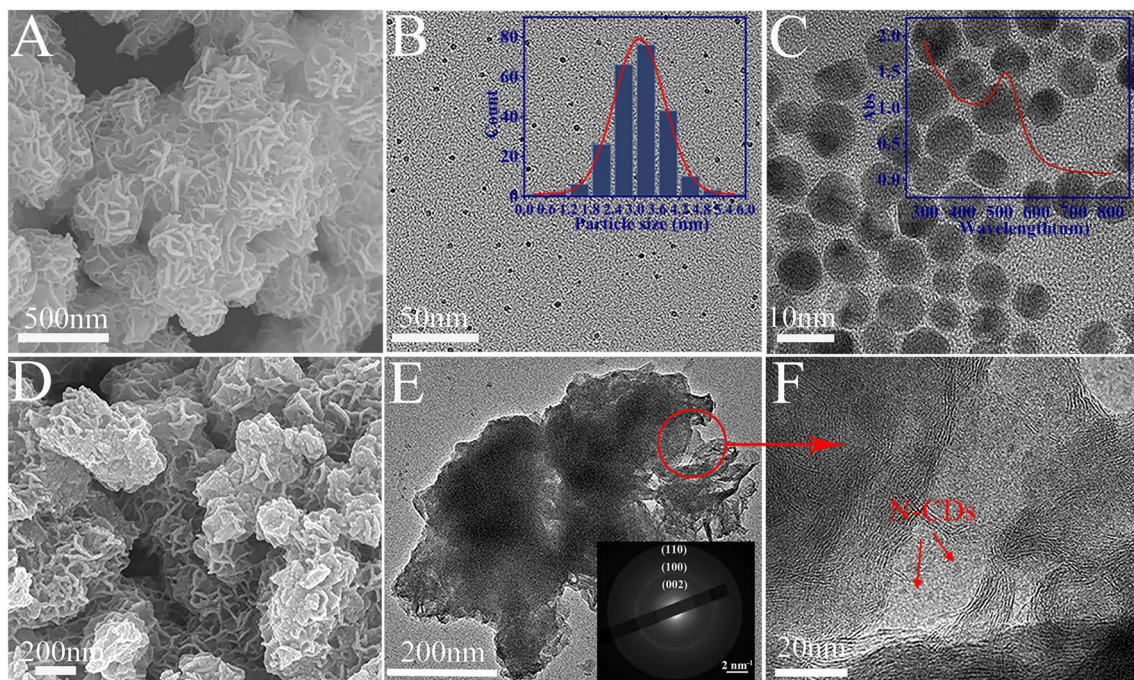


Fig. 1 The morphologies of the prepared materials. SEM image of (A) MoS<sub>2</sub> and (D) MoS<sub>2</sub>@N-CD, TEM image of (B) N-CDs (inset is particle size distribution), (C) GNPs (inset is the absorption spectrum), (E) MoS<sub>2</sub>@N-CDs (inset is the SAED pattern) and (F) partial enlargement of (E).

pattern (SAED) of MoS<sub>2</sub>@N-CDs, and three rings, representing the (002), (100) and (110) crystal planes of MoS<sub>2</sub>, are clearly visible. The TEM image of MoS<sub>2</sub>@N-CDs (Fig. 1E) clearly depicts that MoS<sub>2</sub> exhibits a muslin-like nanosheet layer structure, while N-CDs are uniformly incorporated in MoS<sub>2</sub> nanosheets, thus verifying the successful preparation of the MoS<sub>2</sub>@N-CDs. The introduction of N-CDs is conducive to the enhancement of electrocatalytic performance of the material, which in turn can improve the detection sensitivity.<sup>24</sup>

Further, the XPS and XRD spectra of MoS<sub>2</sub>@N-CDs are displayed in Fig. 2. In the full spectra of MoS<sub>2</sub>@N-CDs (Fig. 2A), five peaks appeared, corresponding to Mo 3d, S 2p, C 1s, N 1s and O 1s, respectively, confirming the existence of C, N, O, Mo and S elements in MoS<sub>2</sub>@N-CDs. Fig. 2B shows the high-resolution spectrum of Mo 3d, the peaks appeared at 228.7 eV and 232.1 eV are ascribed to Mo(IV)3d<sub>5/2</sub> and Mo(IV)3d<sub>3/2</sub> of 1T-MoS<sub>2</sub>, respectively, while the peaks at 229.6 eV and 233.0 eV are assigned to 2H-MoS<sub>2</sub>. According to the proportion of peak area,

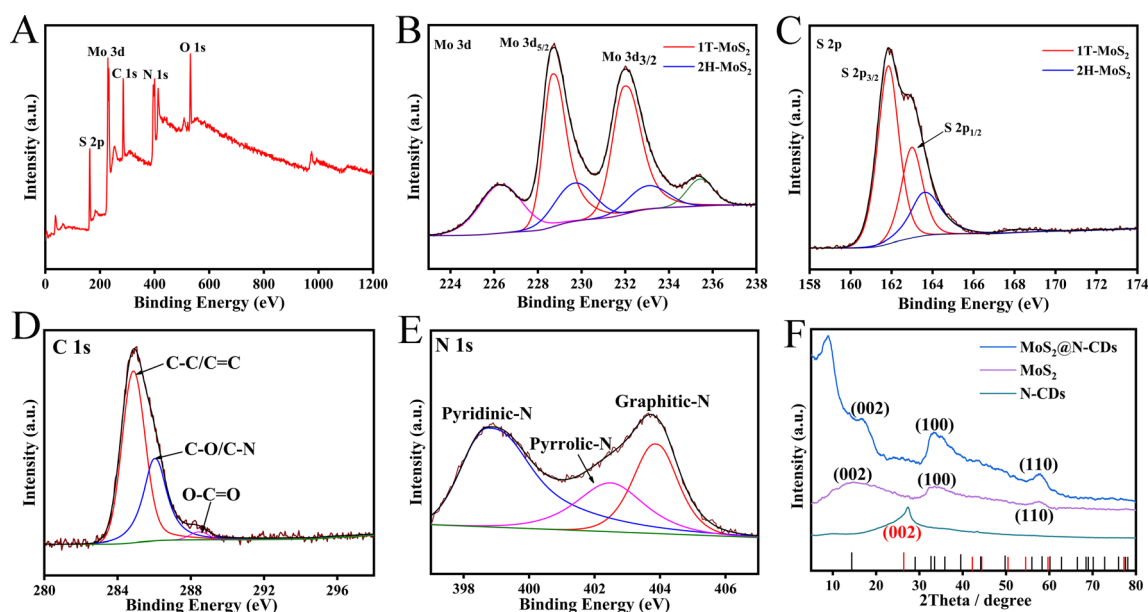


Fig. 2 XPS spectra of (A) MoS<sub>2</sub>@N-CDs, (B) Mo 3d, (C) S 2p, (D) C 1s and (E) N 1s, XRD spectra of N-CDs, MoS<sub>2</sub> and MoS<sub>2</sub>@N-CDs (F).



the content of 1T phase is estimated to be about 76%. In Fig. 2C, the S 2p<sub>3/2</sub> and S 2p<sub>1/2</sub> for 1T-MoS<sub>2</sub> were located at 161.9 and 163.0 eV, respectively. In C 1s spectrum (Fig. 2D), the peaks at 284.8 eV, 286.0 eV and 288.4 eV correspond to C-C/C=C, C-N and C=O, respectively. Among them, the strongest peak at 284.8 eV indicates the existence of graphite C, while the C-N bond suggests the formation of N-CDs. The XPS spectrum of N 1s shows three peaks (Fig. 2E) corresponding to pyridine-N (398.7 eV), pyrrole-N (402.5 eV) and graphite-N (403.9 eV), verifying that the N elements were doped into the carbon dots. Graphite-N can improve the conductivity of MoS<sub>2</sub>@N-CD, and pyridine-N is beneficial for enhancing the electrochemical sensing of organic compounds.<sup>25</sup> Fig. 2F shows the XRD spectra of CDs, MoS<sub>2</sub>, MoS<sub>2</sub>@N-CDs. A broad and relatively intense diffraction peak of N-CDs at  $2\theta = 27.3^\circ$  is assigned to the (002) plane that is slightly shifted from that of graphite ( $2\theta = 26.62^\circ$ ). This is due to the decrease in lattice spacing resulting in a larger angle of the diffraction peaks, which proves that the CDs are doped with nitrogen atoms between the crystal planes.<sup>26</sup> In the XRD pattern of MoS<sub>2</sub>, the three diffraction peaks appearing at  $14.6^\circ$ ,  $31.6^\circ$ , and  $56.1^\circ$  correspond to the (002), (100), and (110) diffraction crystal planes of MoS<sub>2</sub>, respectively. And in the XRD pattern of MoS<sub>2</sub>@N-CDs, three diffraction peaks also appeared, which belonged to the (002), (100) and (110) diffraction crystal planes of MoS<sub>2</sub>. While the diffraction peak appearing at  $8.9^\circ$  corresponded to CDs, which is in accordance with previous report<sup>27</sup> The experimental results of XPS and XRD confirm that MoS<sub>2</sub>@N-CDs were successfully prepared.

### 3.2. Electrochemical characterization of electrodes

CV curves of various electrodes in 5.0 mmol L<sup>-1</sup> K<sub>4</sub>[Fe(CN)<sub>6</sub>]/K<sub>3</sub>[Fe(CN)<sub>6</sub>] solution are displayed in Fig. 3 A. In the scanning range, all electrodes showed a pair of Fe<sup>3+</sup>/Fe<sup>2+</sup> redox peaks. Compared with unmodified GCE (curve a), the anodic peak current (*I*<sub>pa</sub>) and cathodic peak current (*I*<sub>pc</sub>) on MoS<sub>2</sub>/GCE were increased by 1.43-fold and 1.38-fold, respectively, confirming the electrocatalytic effect of MoS<sub>2</sub>. After doped with N-CDs, the peak current values on MoS<sub>2</sub>@N-CDs/GCE continued to increase, indicating N-CDs further improves the electrode performance.

On Au/MoS<sub>2</sub>@N-CDs/GCE (curve d), as a result of the high conductivity of GNPs, *I*<sub>pa</sub> and *I*<sub>pc</sub> continuously increased to 2.17 and 1.95 times of the bare GCE. However, when KdBE and CS were decorated onto the electrode, the current value decreased dramatically (curve e), which was attributed to the non-conducting KdBE and CS hindering the electron transfer.

For more details, the CV curves of different electrodes at various scan rates were recorded in Fig. S2,<sup>†</sup> and it can be observed that the peak current increased with increment of scan rate (*v*). The effective electroactive surface area (*A*) for different electrodes was calculated according to Randles-Sevcik equation (eqn (2)).

$$I_{pa} = 2.69 \times 10^5 n^{3/2} A D^{1/2} C v^{1/2} \quad (2)$$

where *I*<sub>pa</sub> is the anodic peak current, *n* is the number of electrons transferred, *A* (cm<sup>2</sup>) is the electroactive surface area, *D* (cm<sup>2</sup> s<sup>-1</sup>) is the diffusion coefficient, *v* (V s<sup>-1</sup>) is the scan rate and *C* (mol cm<sup>-3</sup>) is redox probe concentration. In the experiment of Fig. S2,<sup>†</sup> *n*, *D* and *C* are equal to 1,  $6.5 \times 10^{-6}$  cm<sup>2</sup> s<sup>-1</sup> and  $5 \times 10^{-6}$  mol cm<sup>-3</sup>, respectively. For different electrodes, the linear regression equations between *I*<sub>pa</sub> and *v*<sup>1/2</sup> were presented in eqn (3)–(6).

$$I_{pa(\text{GCE})} = 174.77 v^{1/2} + 6.59 \quad R^2 = 0.9957 \quad (3)$$

$$I_{pa(\text{MoS}_2/\text{GCE})} = 240.73 v^{1/2} + 14.02 \quad R^2 = 0.9996 \quad (4)$$

$$I_{pa(\text{MoS}_2@\text{N-CDs}/\text{GCE})} = 290.13 v^{1/2} + 18.44 \quad R^2 = 0.9956 \quad (5)$$

$$I_{pa(\text{Au}/\text{MoS}_2@\text{N-CDs}/\text{GCE})} = 369.96 v^{1/2} + 20.13 \quad R^2 = 0.9996 \quad (6)$$

The calculated *A* for GCE, MoS<sub>2</sub>/GCE, MoS<sub>2</sub>@N-CDs/GCE, Au/MoS<sub>2</sub>@N-CDs/GCE is 0.051 cm<sup>2</sup>, 0.070 cm<sup>2</sup>, 0.085 cm<sup>2</sup>, 0.108 cm<sup>2</sup>, respectively. It can be seen that the electroactive surface area of electrodes was significantly increased by modifying MoS<sub>2</sub>@N-CDs and GNPs, which allowed more reactions to occur simultaneously and then resulted in higher electrochemical signals, which undoubtedly contributed to improving the sensitivity of electrochemical analysis.

The influence of material modifications on charge transfer resistance (*R*<sub>ct</sub>) was also studied by AC impedance technique,

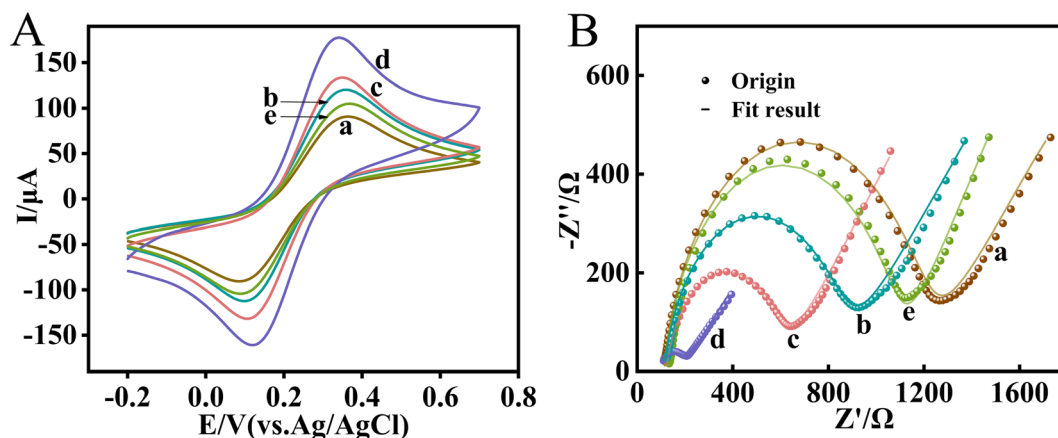


Fig. 3 Cyclic voltammograms (A) and Nyquist curves (B) of different electrodes in 5 mmol L<sup>-1</sup> K<sub>4</sub>[Fe(CN)<sub>6</sub>]/K<sub>3</sub>[Fe(CN)<sub>6</sub>]: (a) GCE, (b) MoS<sub>2</sub>/GCE, (c) MoS<sub>2</sub>@N-CDs/GCE, (d) Au/MoS<sub>2</sub>@N-CDs/GCE, (e) CS/KdBE/Au/MoS<sub>2</sub>@N-CDs/GCE.





the corresponding Nyquist curves was presented in Fig. 3B and fitted by Randles equivalent circuit and the results were listed in Table S1.† The  $R_{ct}$  of unmodified GCE was 1079  $\Omega$ , but  $\text{MoS}_2/\text{GCE}$  showed a smaller semicircle, the corresponding  $R_{ct}$  was reduced to 730.8  $\Omega$ , indicating that  $\text{MoS}_2$  facilitated the electron transport. After modified with  $\text{MoS}_2@\text{N-CDs}$  on the electrode surface, the semicircle diameter decreased even more with  $R_{ct}$  reduced to 482.6  $\Omega$  (curve *c*), demonstrating that the doping of N-CDs effectively improved the conductivity of the nanomaterial. Then, the  $R_{ct}$  decreased rapidly to 95.6  $\Omega$  after continued modification with GNPs (curve *d*), which was attributed to the high conductivity of GNPs. However, on  $\text{CS/KbPE}/\text{Au}/\text{MoS}_2@\text{N-CDs}/\text{GCE}$ , the semicircle diameter increased dramatically and  $R_{ct}$  also increased significantly to 966.9  $\Omega$ , which was due to the weak conductivity of enzyme and CS hindering the electron transfer. The above experimental results show that  $\text{MoS}_2@\text{N-CDs}$  nanocomposites and GNPs can effectively promote the electron transfer efficiency, which enables the electrodes to have a faster current response and thus better sensitivity for electrochemical analysis.

### 3.3. AFM characterization of KdBE loading

The morphology and roughness of electrode surface before and after KdBE loading were inspected using AFM. Images were processed using a Nanoscope Analysis v 1.50 software and were

subjected to second-order flattening. Use root mean square roughness ( $R_q$ ) to evaluate the surface roughness of the sample, as defined below.

$$R_q = \sqrt{\frac{\sum_{i=1}^N (Z_i - Z)^2}{N}} \quad (7)$$

where  $Z_i$  is the height of the  $i$  point with respect to the lowest one in the image and  $N$  is the total number of points comprised in the image.

As can be seen from Fig. 4A–D, the maximum surface height of the electrode was 51.5 nm and the roughness was 18.6 nm before KdBE loading, whereas after KdBE loading, the surface morphology of the electrode was obviously changed, while the maximum surface height increased to 133.9 nm and the surface roughness increased to 27.9 nm, implying that KdBE was loaded onto the electrode.

### 3.4. Electrochemical response of different electrodes to 1-naphthol

Fig. 5A shows the CV curve of  $\text{CS/KdBE}/\text{Au}/\text{MoS}_2@\text{N-CDs}/\text{GCE}$  in 0.1 mol  $\text{L}^{-1}$  PBS with or without 1-NA. In the PBS solution without 1-NA, no oxidation or reduction peak appeared in the CV curve. However, in PBS solutions with 0.8 mM 1-NA, a distinct oxidation peak appeared around 0.48 V, which derived

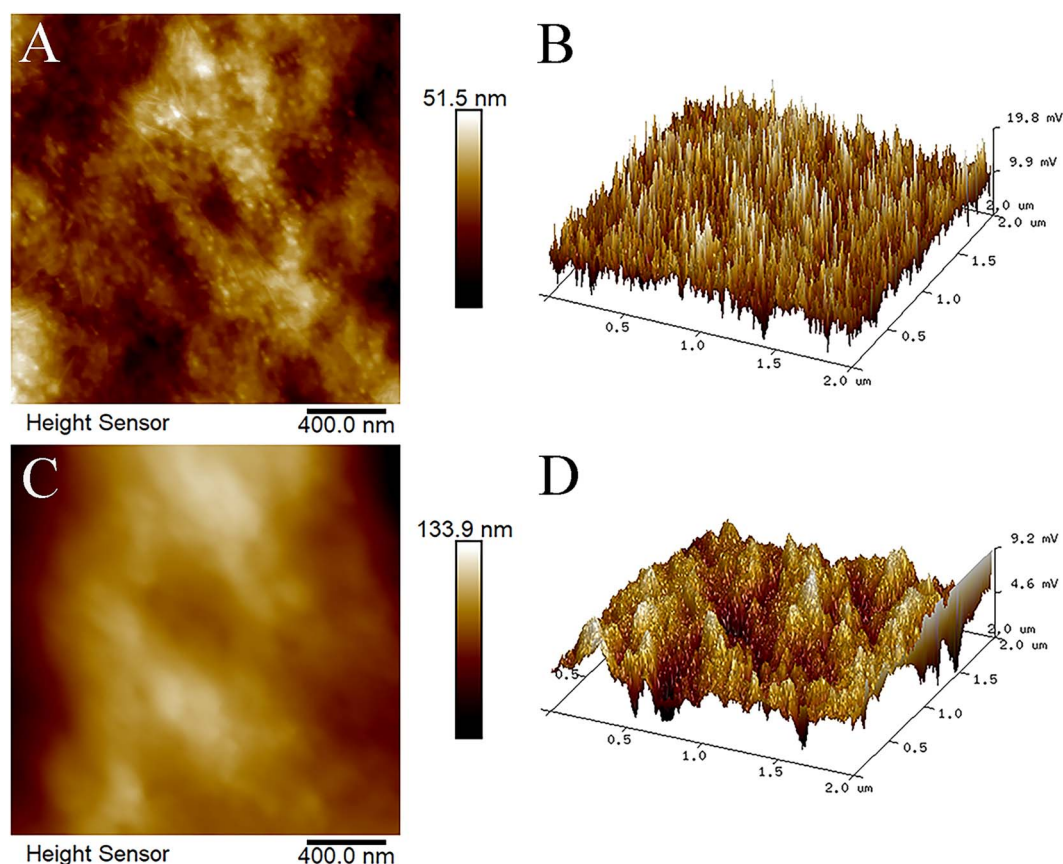


Fig. 4 AFM image of electrode surface: height difference map (A) and surface morphology (B) of  $\text{Au}/\text{MoS}_2@\text{N-CDs}/\text{GCE}$ , height difference map (C) and surface morphology (D) of  $\text{KdBE}/\text{Au}/\text{MoS}_2@\text{N-CDs}/\text{GCE}$ .



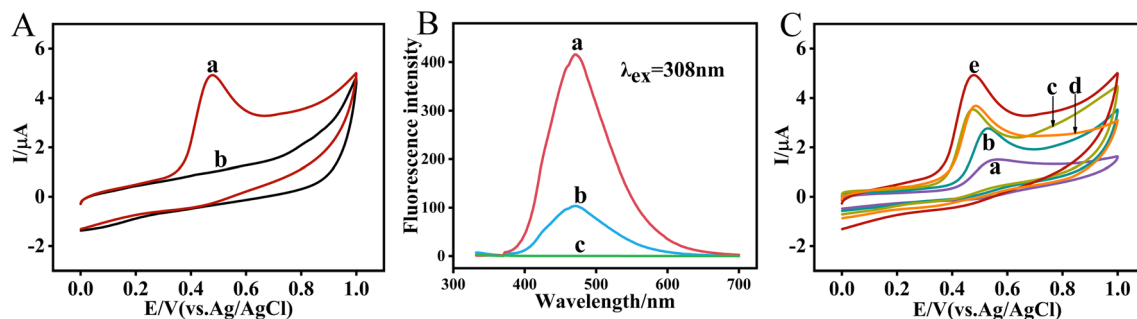


Fig. 5 (A) CV curves of CS/KdBE/Au/MoS<sub>2</sub>@N-CDs/GCE in 0.1 mol L<sup>-1</sup> PBS with 1-NA (a) or without 1-NA (b), (B) Fluorescence spectra of different test systems: (a) PBS solution containing 1-naphthol, (b) PBS solution containing KdBE + 1-NA, (c) PBS solution containing 1-NA, (C) CV curves of different modified electrodes in 0.1 mol L<sup>-1</sup> PBS with 1-NA: (a) CS/KdBE/GCE, (b) CS/KdBE/MoS<sub>2</sub>/GCE, (c) CS/KdBE/MoS<sub>2</sub>@N-CDs/GCE, (d) CS/KdBE/Au/GCE, (e) CS/KdBE/Au/MoS<sub>2</sub>@N-CDs/GCE. Concentrations of 1-NA and 1-naphthol are 0.8 mmol L<sup>-1</sup> and 0.1 mmol L<sup>-1</sup>, respectively.

from the electrochemical oxidation of 1-naphthol produced by KdBE-catalyzed hydrolysis of 1-NA. To confirm the production of 1-naphthol, we collected fluorescence spectra of different reaction systems (Fig. 5B). It can be noticed that no fluorescence emission peak appeared in the PBS system only containing 1-NA, but in the PBS system containing KdBE and 1-NA, a fluorescence emission peak appeared at 470 nm, and the location of the peak was consistent with that of the fluorescence emission peak of 1-naphthol, which proved that KdBE did catalyze the hydrolysis of 1-NA to produce 1-naphthol. Fig. 5A and B also show that KdBE was successfully loaded to the electrode and still had good enzymatic activity.

To examine the effect of the prepared nanomaterials on 1-naphthol sensing signals, the CV responses of various modified electrodes in 0.1 M PBS containing the same concentration of 1-NA were tested (Fig. 5C). It is observed that although the oxidation peak of 1-naphthol appeared on all electrodes, the smallest peak current ( $I_p$ ) was obtained on the electrode without nanomaterials modification (curve a), whereas the  $I_p$  on CS/KdBE/MoS<sub>2</sub>/GCE (curve b) was significantly increased to 1.99 folds of that on CS/KdBE/GCE. When modified with MoS<sub>2</sub>@N-CDs, the  $I_p$  increased to 2.74 times that of CS/KdBE/GCE (curve c), which reconfirmed that MoS<sub>2</sub>@N-CDs is a good electrocatalyst to effectively amplify the electrochemical oxidation signal of 1-naphthol. When modified with GNPs, the  $I_p$  of CS/KdBE/Au/GCE was 2.79 times higher than that of CS/KdBE/GCE, suggesting that GNPs can also enhance the electrical signals. Under the synergistic effect of MoS<sub>2</sub>@N-CDs and GNPs, the highest  $I_p$  was obtained on CS/KdBE/Au/MoS<sub>2</sub>@N-CDs/GCE (curve d), which was 3.43 times higher than that on CS/KdBE/GCE. The above experimental results indicate that the constructed electrochemical sensing platform has good response sensitivity and promises to achieve highly sensitive detection of pesticide.

### 3.5. Optimization of experimental parameters

The influence of solution pH upon current response was firstly investigated. The results in Fig. 6A showed that  $I_p$  reached the maximum at pH 7.0, indicating the enzyme catalyzed by KdBE is most effective at pH 7.0. Then, the effect of MoS<sub>2</sub>@N-CDs amount was optimized (Fig. 6B). With the increase of

MoS<sub>2</sub>@N-CDs loading on the electrode, the  $I_p$  firstly showed an upward trend, reaching the maximum at 20  $\mu$ L, and then decreased. As a result, 20  $\mu$ L of 1 mg mL<sup>-1</sup> MoS<sub>2</sub>@N-CDs was chosen as the optimal amount.

Fig. 6C shows the influence of GNPs loading on  $I_p$ , with the increase of GNPs loading, the  $I_p$  rose accordingly until it reached the maximum at 12  $\mu$ L. Later on, with the increase of GNPs loading, the  $I_p$  decreased instead. This is because that GNPs has high conductivity and catalytic activity.<sup>28</sup> Within a certain range, more GNPs is favorable for the oxidation of 1-naphthol. However, too much GNPs may agglomerate and form a thick film, which is rather unfavorable to the electron transfer at the electrode interface and consequently leads to a decrease in the current response. So, 12  $\mu$ L was selected as the optimal loading volume of GNPs.

The optimization results of KdBE dosage are shown in Fig. 6D.  $I_p$  increased with increasing KdBE dosage, but decreased above 0.19 U. This is because more KdBE can generate more 1-naphthol and then produce a larger electrochemical signal. However, as non-conducting protein, enzyme loading can enlarge the resistance of the modified electrode and hinder electron transfer,<sup>29</sup> which will result in a decrease in current response. The combination effect of the two aspects gave 0.19 U as the optimum enzyme dosage.

The influence of the enzyme-substrate interaction time is shown in Fig. 6E. As the reaction time prolonged, more 1-naphthol was generated and the  $I_p$  increased accordingly, but  $I_p$  value did not change much after 5 min, indicating that the enzymatic reaction reached equilibrium and then an optimal reaction time of 5 min was chosen.

Finally, the incubation time of CPF with KdBE was optimized (Fig. 6F). It was observed that  $I_p$  decreased with the increase of incubation time, but almost kept the same after 15 min, indicating that the effect of CPF on KdBE basically reached equilibrium. Therefore, 15 min was chosen as the optimal incubation time.

### 3.6. CPF detection

Under optimal experimental conditions, the detection performance of the developed sensor on CPF was examined by SWV. It can be observed that the oxidation peak current obtained in the



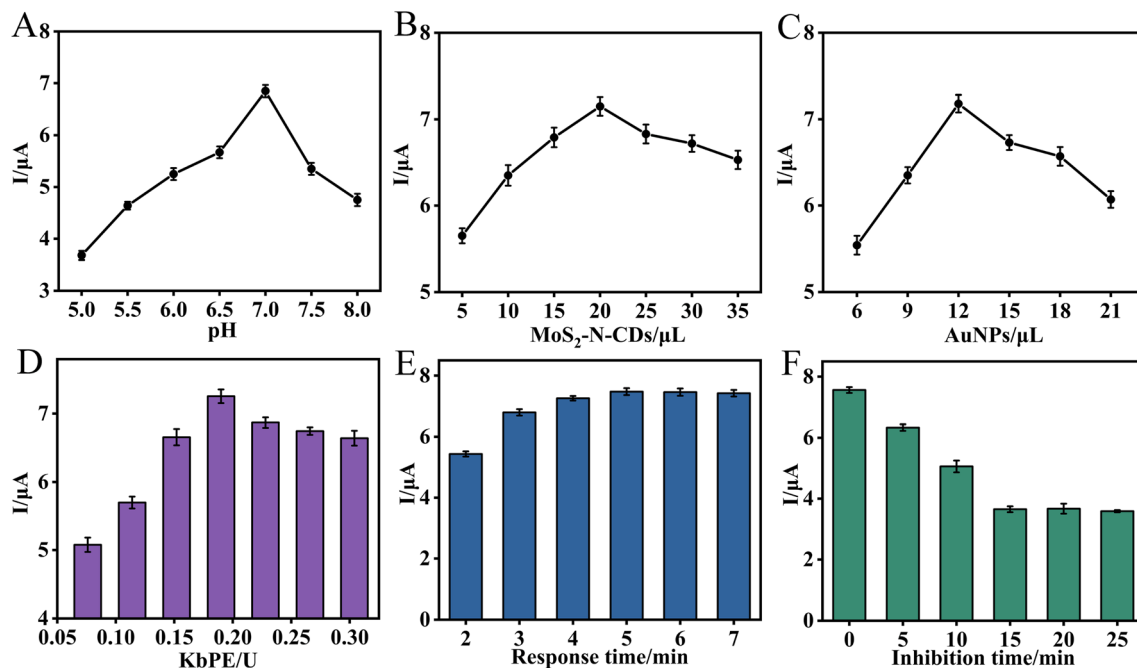


Fig. 6 Optimization of experimental parameters: (A) pH, (B)  $\text{MoS}_2\text{-N-CDs}$  loading, (C) GNPs loading, (D) KdBE dosage, (E) effect of KdBE and 1-NA interaction time on peak current, (F) effect of CPF and KdBE incubation time on peak current.

absence of CPF was the highest, which gradually decreased with the increase of CPF concentration (Fig. 7A). The experiments in Fig. 5 confirmed that KdBE can catalyze the hydrolysis of 1-NA to produce 1-naphthol (Fig. 5B), which is an electrically active substance that can be electrocatalytically oxidized to generate an oxidation peak (Fig. 5A). The more 1-naphthol is present, the higher the peak current is generated. Thus, the experimental results shown in Fig. 7A indicate that the bioactivity of KdBE was inhibited when CPF existed, resulting in less 1-naphthol production. And the more CPF there is, the stronger the inhibition of KdBE activity, and then the less 1-naphthol was produced, causing a lower oxidation peak current.

Taking the inhibition rate ( $\Delta I\%$ ) of CPF on current signals as the quantitative index, a linear correlation was observed between  $\Delta I\%$  and the logarithm of CPF concentration ( $\lg C$ ) in the range of 0.01–500  $\mu\text{g L}^{-1}$ . The linear equation was  $\Delta I(\%) = 10.03 \lg C + 32.48$  ( $R^2 = 0.9921$ ) (eqn (7)), and the limit of detection (LOD) was  $3.5 \times 10^{-3} \mu\text{g L}^{-1}$  ( $S/N = 3$ ).

Table 1 compares the method in this work with previously reported CPF detection methods. It can be noticed that the proposed method has a wide linear range and the LOD value is comparable or even lower. More advantageously, the detection is based on the changes in the electrical signal caused by CPF,

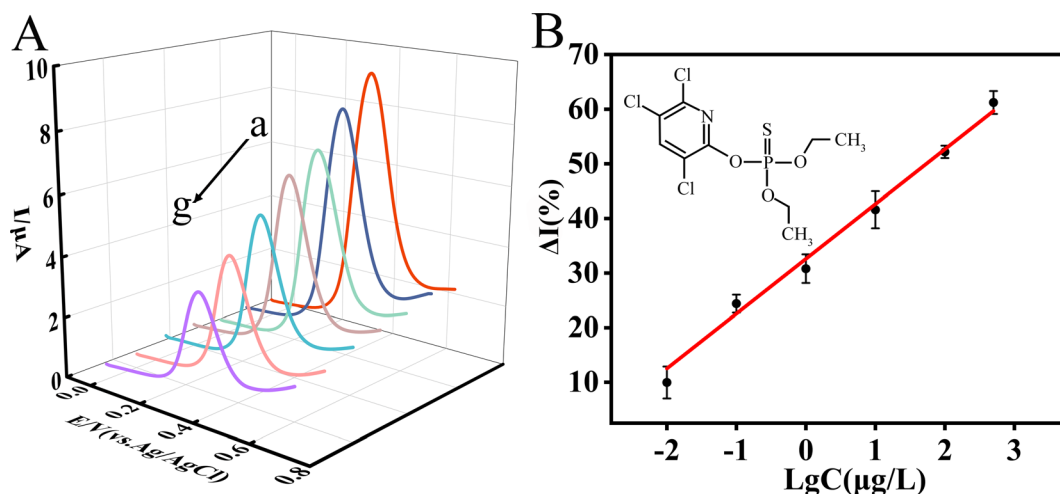


Fig. 7 (A) SWV curves of CS/KdBE/Au/ $\text{MoS}_2\text{-N-CDs}$ /GCE in PBS with 1-NA (0.8 mM) after incubation with different concentrations of CPF (a–g: 0, 0.01, 0.1, 1, 10, 100, 500  $\mu\text{g L}^{-1}$ ), (B) linear relationship between  $\Delta I\%$  and  $\lg C$ .





Table 1 Comparison of the proposed method with other reported methods

Method	Linear rang (mol L <sup>-1</sup> )	LOD (mol L <sup>-1</sup> )	Ref.
MSPE/GC-MS	$1.99 \times 10^{-10}$ – $1.4 \times 10^{-6}$	$5.71 \times 10^{-11}$	30
MSPE-GC- $\mu$ ECD	$8.56 \times 10^{-10}$ – $5.70 \times 10^{-7}$	$2.28 \times 10^{-10}$	31
SPME-HPLC-UV	$7.13 \times 10^{-10}$ – $5.70 \times 10^{-7}$	$2.14 \times 10^{-10}$	32
HPLC-UV	$1.14 \times 10^{-8}$ – $7.13 \times 10^{-7}$	$2.28 \times 10^{-9}$	33
Colorimetry	$1.43 \times 10^{-9}$ – $2.28 \times 10^{-5}$	$5.99 \times 10^{-8}$	34
Spectrophotometry	$2.50 \times 10^{-8}$ – $2.50 \times 10^{-6}$	$6.50 \times 10^{-9}$	35
Immunosensor	$2.85 \times 10^{-11}$ – $1.43 \times 10^{-7}$	$2.11 \times 10^{-11}$	36
ECL	$1.00 \times 10^{-14}$ – $1.00 \times 10^{-9}$	$6.23 \times 10^{-17}$	37
CNTf-AgNPs/PGE	$2.50 \times 10^{-7}$ – $5.00 \times 10^{-5}$	$5.33 \times 10^{-7}$	38
MnFe-MOF/SPE	$1.00 \times 10^{-9}$ – $1.00 \times 10^{-7}$	$8.50 \times 10^{-10}$	39
Au@CeO <sub>2</sub> /ITO	$1.00 \times 10^{-11}$ – $5.00 \times 10^{-7}$	$1.20 \times 10^{-13}$	40
Rod-CeO <sub>2</sub> /CA/GCE(PAM-Cl)	$5.00 \times 10^{-11}$ – $1.00 \times 10^{-7}$	$3.40 \times 10^{-12}$	41
CNFs/GO/CS-GO/ACH/SPCE	$2.50 \times 10^{-9}$ – $1.00 \times 10^{-6}$	$2.20 \times 10^{-9}$	13
CuNWs/rGO/SPCE	$2.85 \times 10^{-8}$ – $5.70 \times 10^{-7}$	$8.84 \times 10^{-9}$	14
CS/KdBE/GNPs/MoS <sub>2</sub> @N-CDs/GCE	$2.85 \times 10^{-11}$ – $1.43 \times 10^{-6}$	$9.98 \times 10^{-12}$	This work

thus effectively overcoming the interference of the food matrix's color on the determination.

### 3.7. Reproducibility, stability and anti-interference capability

Under the same test conditions, RSD of the peak current values obtained from five individual CS/KdBE/Au/MoS<sub>2</sub>@N-CDs/GCE measured in PBS containing 0.8 mM 1-NA was 4.02%. Meanwhile, the same CS/KdBE/Au/MoS<sub>2</sub>@N-CDs/GCE was repeatedly measured in PBS containing 0.8 mM 1-NA for five times, and the RSD of the peak currents was 2.69%. The above results show that the proposed sensor has a satisfactory reproducibility.

The storage stability of CS/KdBE/Au/MoS<sub>2</sub>@N-CDs/GCE was investigated (Fig. 8A). The results showed that for the same concentration of 1-NA, the current response of the sensors decreased to 91.2% of the initial peak current after 15 days of storage and to 79.7% after 30 days, indicating that the sensors have good storage stability. The influence of possible co-existing substances and other types of pesticides on CPF assay was studied (Fig. 8B). Taking the peak current obtained only in the presence of 30  $\mu$ g L<sup>-1</sup> CPF as 100%, 300  $\mu$ g L<sup>-1</sup> ascorbic acid,

citric acid, glucose, oxalic acid, urea, NaCl, MgCl<sub>2</sub>, FeCl<sub>3</sub>, Na<sub>2</sub>SO<sub>4</sub>, NaNO<sub>2</sub>, and 30  $\mu$ g L<sup>-1</sup> of lindane and deltamethrin did not have significant influence on the peak current signals, which indicated that the constructed sensor had acceptable selectivity.

### 3.8. Actual sample assay

To verify the practicability of the proposed method, oilseed rape and cabbage bought from local farmers' markets were used for actual tests. First, 10 g of sample was cut into small pieces and extracted with 100 mL water for 5 min, followed by centrifugation for 10 min at 8000 rpm, the supernatant was collected and diluted 100 times with PBS 7.0 as actual samples for detection and no CPF was found. Subsequently, the recoveries of CPF spiked in the samples were measured, and each spiked concentration was tested three times in parallel, the results are presented in Table 2. As shown, the spiked recoveries of CPF were in the range of 98.09% to 106.01%, with RSDs in the range of 2.20% to 5.23%. Table S2† compares the assay performance of different CPF detection methods for real samples. It was found that the recoveries and RSD values of this work were

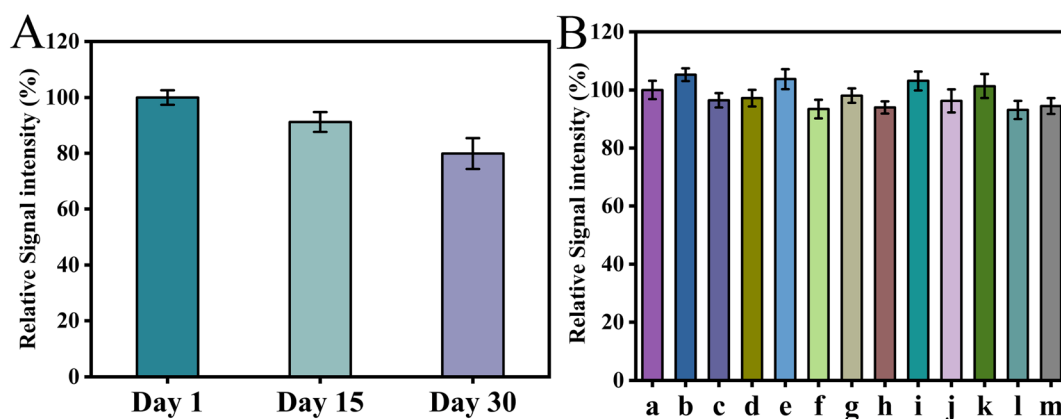


Fig. 8 (A) Storage stability of CS/KdBE/Au/MoS<sub>2</sub>@N-CDs/GCE, (B) anti-interference capability of CS/KdBE/Au/MoS<sub>2</sub>@N-CDs/GCE: (a) CPF, (b) ascorbic acid, (c) citric acid, (d) glucose, (e) oxalic acid, (f) urea, (g) NaCl, (h) MgCl<sub>2</sub>, (i) FeCl<sub>3</sub>, (j) Na<sub>2</sub>SO<sub>4</sub>, (k) NaNO<sub>2</sub>, (l) lindane, (m) deltamethrin.

Table 2 Detection results of CPF in actual samples

Samples	Added ( $\mu\text{g L}^{-1}$ )	Found ( $\mu\text{g L}^{-1}$ )	Recoveries (%)	RSD% ( $n = 3$ )
Oilseed rape	10	10.60	106.01	3.91
	50	49.23	98.47	2.31
	250	255.15	102.06	3.15
Cabbage	10	10.57	105.69	5.23
	50	51.89	103.79	3.38
	250	245.21	98.09	2.20

within reasonable ranges. This indicates that the proposed sensor is suitable for detecting CPF in real samples.

## 4. Conclusion

In this work, a new enzyme-inhibited electrochemical biosensor was developed for the highly sensitive detection of CPF using  $\text{MoS}_2/\text{N-CDs}$  as the electrocatalyst and KdBE as the biorecognition element for CPF. Thanks to the sensing signal amplification effect of nanomaterials and the high susceptibility of KdBE to CPF, the fabricated enzyme electrode exhibited superior sensing performance with a LOD of  $3.5 \times 10^{-3} \mu\text{g L}^{-1}$ . Since the response mechanism of the sensor is based on the change of current signal caused by the inhibition of KdBE activity by CPF, the interference of sample color on the assay can be eliminated effectively. What's more, the proposed sensing method has the advantages of simplicity of operation and affordability, enabling its application for widespread screening of CPF residue in diverse various agri-food samples.

## Author contributions

Jiayu Chen: methodology, data curation, validation, writing-original draft. Chun Ji: supervision, validation. Xiao Wang: formal analysis, investigation. Yunxia Tian: investigation, visualization. Tao Han: methodology, conceptualization, writing-review & editing, supervision, funding acquisition.

## Conflicts of interest

The authors declare that they have no known competing financial interests or personal relationships that could have appeared to influence the work reported in this paper.

## Acknowledgements

This work was financially supported by Guizhou Provincial Science and Technology Project (QKHJC-ZK [2022] Key015), National Natural Science Foundation of China (32160603).

## References

- X. Wang, S. Ai, A. Xiong, W. Zhou, L. He, J. Teng, X. Geng and R. Wu, *Anal. Methods*, 2023, **15**, 6266–6274.
- R. Lyu, Y. Lei, C. Zhang, G. Li, R. Han and L. Zou, *Anal. Chim. Acta*, 2023, **1275**, 341579.
- P. Krishna Perumal, C.-w. Chen, B. S. Giri, R. R. Singhanian, A. K. Patel and C.-D. Dong, *J. Food Sci. Technol.*, 2023, **61**, 631–641.
- M. R. Moghadam, B. Zargar and S. Rastegarzadeh, *Analyst*, 2018, **143**, 2174–2182.
- V.-T. Nguyen, L.-H. Tran, T.-K. Van and D.-V. Le, *J. Anal. Chem.*, 2022, **77**, 604–610.
- Y. Xiong, J. Huang, R. Wu, X. Geng, H. Zuo, X. Wang, L. Xu and S. Ai, *Appl. Spectrosc.*, 2023, **77**, 160–169.
- S. Ghosh, A. R. Gul, C. Y. Park, M. W. Kim, P. Xu, S. H. Baek, J. R. Bhamore, S. K. Kailasa and T. J. Park, *Chemosphere*, 2021, **279**, 130515.
- Y. Dong, R. Chen, L. Wu, X. Wang, F. Jiang, Z. Fan, C. Huang and Y. Chen, *Biosens. Bioelectron.*, 2022, **207**, 114127.
- Z. Chen, L. Zhao, Z. Zhang, J. Wu, L. Zhang, X. Jing and X. Wang, *Talanta*, 2023, **265**, 124802.
- M. A. Kamyabi and M. Moharramnezhad, *Anal. Methods*, 2022, **14**, 750–762.
- R. Ding, W. Jiang, Y. Ma, Q. Yang, X. Han and X. Hou, *Microchem. J.*, 2023, **187**, 108425.
- W. Guo, L. Liang, Y. Zhao, C. Zhao, X. Lu, Y. Cao and F. Gao, *Colloids Surf., B*, 2023, **224**, 113238.
- W. S. T. Tun, A. Saenchoopa, S. Daduang, J. Daduang, S. Kulchat and R. Patramanon, *RSC Adv.*, 2023, **13**, 9603–9614.
- J. Suwannachai, A. Saenchoopa, W. S. T. Tun, R. Patramanon, S. Daduang, J. Daduang and S. Kulchat, *Food Chem.*, 2024, **434**, 137431.
- H. Tao, F. Liu, C. Ji, Y. Wu, X. Wang and Q. Shi, *RSC Adv.*, 2022, **12**, 5265–5274.
- J. Bao, C. Hou, M. Chen, J. Li, D. Huo, M. Yang, X. Luo and Y. Lei, *J. Agric. Food Chem.*, 2015, **63**, 10319–10326.
- Q. Luo, L. Sun, Y. Zhao, C. Wang, H. Xin, D. Li and F. Ma, *J. Mater. Sci. Technol.*, 2023, **145**, 165–173.
- L. Wang, Z. Fan, F. Yue, S. Zhang, S. Qin, C. Luo, L. Pang, J. Zhao, J. Du, B. Jin and H. Zhang, *Food Chem.*, 2024, **430**, 137027.
- X. Ma, J. Yu, L. Wei, Q. Zhao, L. Ren and Z. Hu, *Talanta*, 2023, **253**, 123959.
- S. Senapati, R. Naik, S. Dash, A. Mohanty, K. Braeckmans, S. C. De Smedt and S. K. Samal, *ACS Sustainable Chem. Eng.*, 2023, **11**, 13535–13544.
- K. Das, A. Uppal and R. K. Saini, *Spectrochim. Acta, Part A*, 2016, **152**, 378–383.
- L. Yang, D. Huo, C. Hou, K. He, F. Lv, H. Fa and X. Luo, *Process Biochem.*, 2010, **45**, 1664–1671.
- W. Haiss, N. T. K. Thanh, J. Aveyard and D. G. Fernig, *Anal. Chem.*, 2007, **79**, 4215–4221.
- F. Shalali, S. Cheraghi and M. A. Taher, *Mater. Chem. Phys.*, 2022, **278**, 125658.
- M. Nanthagopal, P. Santhoshkumar, N. Shaji, S. Praveen, H. S. Kang, C. Senthil and C. W. Lee, *Appl. Surf. Sci.*, 2019, **492**, 871–878.
- H. Afshary, M. Amiri, A. Bezaatpour and M. Wark, *J. Electrochem. Soc.*, 2022, **169**, 026523.



- 27 H. M. El Sharkawy, A. S. Dhmees, A. R. Tamman, S. M. El Sabagh, R. M. Aboushahba and N. K. Allam, *J. Energy Storage*, 2020, **27**, 101078.
- 28 D. Orenli, C. K. Selvi, F. Ozturk, P. E. Erden and E. Kilic, *Anal. Biochem.*, 2023, **662**, 115002.
- 29 Y. Li, L. Shi, G. Han, Y. Xiao and W. Zhou, *Sens. Actuators, B*, 2017, **238**, 945–953.
- 30 M. Samadifar, Y. Yamini and M. M. Khataei, *J. Food Compos. Anal.*, 2023, **118**, 105158.
- 31 H. Sereshti, A. Amirafshar, A. Kadi, H. Rashidi Nodeh, S. Rezaia, H. Y. Hoang, A. Barghi and Y. Vasseghian, *Chemosphere*, 2023, **320**, 138065.
- 32 X. Wang, J. Yang, J. Zhao, Z. Zhou, X. Du and X. Lu, *Chin. J. Chromatogr.*, 2022, **40**, 910–920.
- 33 Z. Bahirae, S. Fathi and M. Safari, *Environ. Prog. Sustainable Energy*, 2023, **42**, e13971.
- 34 W. Jiang, Z. Yang, F. Tong, S. Zhang, L. Zhu, L. Wang, L. Huang, K. Liu, M. Zheng, Y. Zhou, R. Hou and Y. Liu, *Biosens. Bioelectron.*, 2023, **224**, 115074.
- 35 N. B. Tran, Q. K. Nguyen, T. V. Vu, A. Q. Hoang, T. D. Pham, D. T. Pham, T. A. H. Nguyen and T. N. M. Pham, *Colloid Polym. Sci.*, 2023, **301**, 239–250.
- 36 Y. Wang, A. M. Abd El-Aty, S. Wang, X. Cui, J. Zhao, X. Lei, L. Xu, Y. She, F. Jin, J.-B. Eun, J.-H. Shim, J. Wang, M. Jin and B. D. Hammock, *Food Chem.*, 2023, **413**, 135607.
- 37 Z. Sun, J. Lu, X. Zhang, X. Shan, Q. Wu, C. Li, H. Li, S. Yang and L. Tian, *Microchim. Acta*, 2022, **189**, 473.
- 38 L. S. Porto, L. F. Ferreira, W. T. Pio dos Santos and A. C. Pereira, *Talanta*, 2022, **246**, 123477.
- 39 P. Janjani, U. Bhardwaj, R. Gupta and H. S. Kushwaha, *Anal. Chim. Acta*, 2022, **1202**, 339676.
- 40 G. B. V. S. Lakshmi, M. Poddar, T. K. Dhiman, A. K. Singh and P. R. Solanki, *Colloids Surf., A*, 2022, **653**, 129819.
- 41 X. Zhang, W. Zhang, J. Du, Q. Sun, W. Yuan, H. Wang and J. Wu, *Microchem. J.*, 2023, **191**, 108891.

